Hernández-Jiménez, F., Soria-Verdugo, A., Acosta-Iborra, A. & Santana, D. (2019). Exergy recovery from solar heated particles to supercritical CO2. *Applied Thermal Engineering*, vol. 146, pp. 469–481.

Exergy recovery from solar heated particles to supercritical CO_2

F. Hernández-Jiménez[a,*], A. Soria-Verdugo[a], A. Acosta-Iborra[a], D. Santana[a]

[a]*Universidad Carlos III of Madrid, Department of Thermal and Fluid Engineering. Av. de la Universidad, 30, 28911, Leganés, Madrid, Spain*

Abstract

In this work, the technical feasibility of a fluidized and a fixed bed heat exchanger in a concentrating solar power (CSP) tower for heat recovery applications is analysed using Two-Fluid Model simulations. The heat recovery process analysed in this work corresponds to the discharge of sensible heat from solid particles. In the cases studied, the fluidizing agent of the bed is carbon dioxide (CO_2) in supercritical conditions and the particles, which constitute the bed material, are sensible heat storage material. CO_2 is gaining attention in its application as a working fluid in thermodynamic cycles for power generation, especially in transcritical and supercritical conditions due to its high density and excellent heat transfer characteristics. Currently, research is focused on exploring the CO_2 capabilities when used in combination with CSP technologies, together with systems that allow the storage and recovery of the solar thermal energy.

Fixed or fluidized beds work as a direct contact heat exchanger between the particles and the working fluid that percolates through the bed material. Several bed configurations are presented to derive the optimal configuration of the bed that enhances the efficiency from both the energetic and the exergetic points of view. The results indicate that a fixed bed heat exchanger produces a maximum increase of availability in the CO_2 flow during longer times than a fluidized bed heat exchanger. Therefore, to maximise the exergy recovery from solar heated particles to supercritical CO_2 a fixed bed heat exchanger is more suitable than a fluidized bed heat exchanger.

Keywords: Supercritical carbon dioxide; fluidized bed; fixed bed; heat exchanger; concentrating solar power.

1. Introduction

In the last decades, the use of solar energy as a renewable alternative to fossil fuels for power generation has received great impulse. Solar energy is an ubiquitous, clean, and readily accessible renewable energy source. Concentrating Solar Power (CSP) technologies are an important alternative for providing clean and renewable electricity in the present and in the future. CSP can be integrated with large thermal storage

---

*Corresponding author. Tel:+34 91 624 8344

Email address: `fhjimene@ing.uc3m.es` (F. Hernández-Jiménez)

systems to store part of the energy captured during the day to be used along the night or during cloudy days. Storage systems can also soften the short period fluctuations of the energy captured as a consequence of the transient blockage of the sun by a cloud. Besides, CSP offers the possibility of hybridization of CSP with fossil fuels [1]. Central receivers, located at the top of the tower, absorb the incident radiation from the heliostat field and are considered to be the most critical element in CSP technology. Current central receiver technologies typically employ either water/steam or molten nitrate salt as heat transfer fluid [2]. The input temperatures of the working fluid in the receiver should be maximized to enhance the thermal-to-electric efficiency of the power cycles. However, at temperatures above 600 ^oC, molten nitrate salt becomes chemically unstable, producing oxide ions that are highly corrosive, which results in a significant salt consumption and increses the damage to the central receiver [3].

Recently, carbon-dioxide (CO_2) is becoming an attractive working−fluid for thermodynamic power cycles due to several reasons: it is inexpensive, capable of withstanding very high temperatures, non−toxic, non−combustible, non−explosive, and abundant [4, 5]. CO_2 also has a moderate critical pressure (7.38 MPa) and critical temperature (31.1 ^oC). Because of that, interest in the use of supercritical-CO_2 as a working−fluid for power cycles has been growing lately especially in the contexts of waste−heat recovery, solar thermal and nuclear power generation [6, 7, 8]. Ortega et al. [9] analysed the thermal and mechanical stresses of the tubes of a tubular receiver containing CO_2 in supercritical conditions and concluded that the tubes can work during the lifetime of the receiver. Furthermore, the high density of CO_2 near the critical point allows to minimize compressor work, yielding a potentially higher cycle efficiency. In addition, these supercritical systems are projected as compact cycles to have a smaller weight, volume and thermal mass inertia, reducing the complexity of the power block compared to Rankine cycles. The realization of these designs may also result in reduced installation, maintenance and operation costs of the system [10]. Cycles based on carbon dioxide has been already proposed as an alternative for central receiver solar power plants, either as Brayton or combined Brayton−Organic Rankine Cyles [11]. In this regard, Wang et al. [12] performed a detailed analysis of the different possibilities of Brayton cycles using supercritical CO_2 for solar power tower plants. They concluded that the inter-cooling cycle layout and the partial-cooling cycle layout can generally yield the best performances. They proposed the use of novel molten salts capable of exceeding the current limit of 650 ^oC as in the receiver to transfer heat to the CO_2.

Furthermore, some studies consider the thermal energy storage unit in CO2 based power generation systems. Osorio et al. [13] considered a molten salt tank for thermal energy storage which was charged with CO_2. Liu et al. [14] proposed a spherical granite packed bed instead and Zhang et al. [15] incorporated different storage units to the CO_2 system where energy was accumulated either as sensible and latent heat, using CO_2 as working fluid, both at high and low pressure. None of the studies analysed in detail the thermal behaviour of the thermal energy storage system, but the overall efficiency of the plant (receiver, power block, etc.). Recently, Johnson et al. [16] numerically analysed the performance of a packed bed thermal energy

storage system with supercritical CO_2 as working fluid. The system allows to store 70000 kWh in a huge system with storage times of several hours. Their system was fed laterally neglecting buoyancy effects and they obtained fractional exergetic efficiencies of around 80% for the cases studied.

Figure 1 sketches a possible configuration of a solar power plant using a regenerative Brayton cycle. In the sketch, the working fluid of the Brayton cycle (CO_2 in supercritical conditions) is directly heated in the receiver and a storage tank is proposed. The tank would be charged when the energy available at the receiver is more than enough to supply the cycle and would be discharged when the energy capture in the receiver cannot fulfil the demand of the cycle. Among the different possibilities for thermal storage in concentrated solar power plants [17], the storage tank proposed is composed of a granular material which will exchange heat by direct contact with the working fluid. Depending on the velocity of the working fluid, the bed material conforming the storage system can be under fluidized or fixed conditions. Fixed bed configurations have been widely studied for thermal energy storage, either as sensible heat or latent heat [17]. For example, Hänchen et al. [18] and Zanganeh et al. [19] studied, experimentally and numerically, a fixed bed of rocks for high temperature storage fluidized with air at ambient pressure. Anderson et al. [20] and Opitz and Treffinger [21] also developed numerical models to simulate packed beds at moderated and high temperature, respectively, both again using air at ambient pressure. Cascetta et al. [22] performed CFD simulations and experimental measurements for a packed bed with air up to 300 ^{o}C. They concluded the importance of considering temperature dependant properties in the simulation. In the present work, both configurations, fixed and fluidized bed, will be studied to maximize the heat recovery from an exergetic point of view.
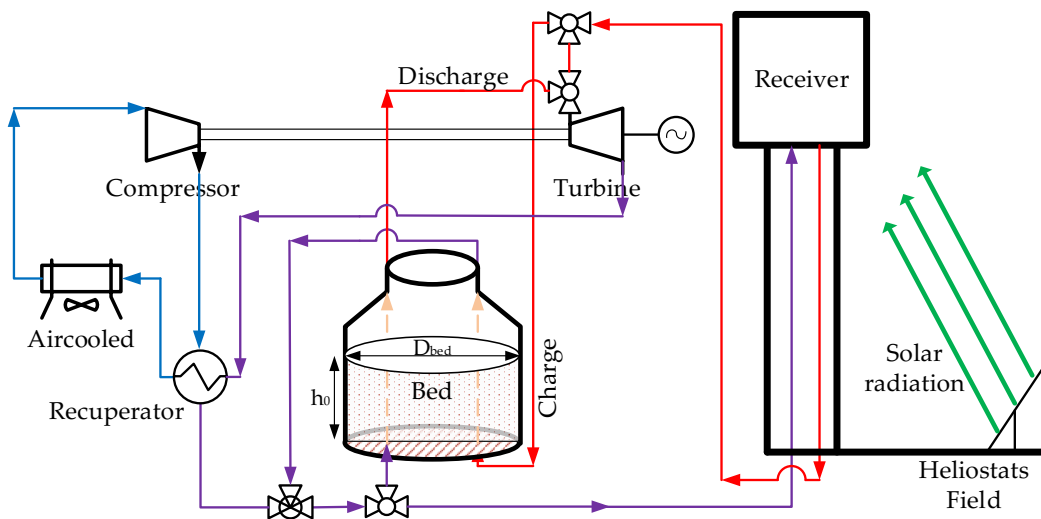

Figure 1: Sketch of solar power plant with particles storage tank.

3

Furthermore, an alternative to Figure 1 configuration or to the use of molten salts, the particles employed in a storage tank of a CSP plant could be directly those of a particle receiver, i.e., direct particle heating [23]. Compared to the system described in Figure 1, direct particle heating would lead to higher system efficiencies since this configuration requires no heat exchanger to recover the heat absorbed in the receiver to the particles of the storage system, which may induce certain heat losses. However, the usage of direct particle heating involves the particle receiver working pressurized and this would imply a more complicated operation of the plant. Particle receivers are currently designed and tested to achieve higher operating temperatures with potential to increase the maximum temperature of the heat transfer media above $1000^{o}C$ and to increase the receiver efficiency. Besides, they can constitute inexpensive direct storage and can also be used to produce thermochemical reactions and process heat [24]. Specifically, in dense particle suspension (DPS) receivers, particles are forced to ascend through the receiver tubes and then the heated particles are stored and recirculated using fluidized bed systems [25, 26, 27, 28, 29, 30].

In the field of fluidization, very few attempts have been done to use CO_2 in supercritical conditions as a fluidizing agent. Poletto et al. [31] fluidized a bed of particles with CO_2 in several conditions to analyse the differences between gas-solid fluidization and more alike liquid-solid fluidization when the temperature and pressure of the CO_2 where close to supercritical conditions. Marzocchella and Salatino [32] and Vogt et al. [33] reached the supercritical conditions of CO2 to analyse experimentally the fluid dynamics of the bed. Using water in supercritical conditions instead of CO_2, Wei and Lu [34] and Lu et al. [35] analysed the fluidization behaviour of a bed based on pressure fluctuations and heat transfer between bed and wall, respectively. Rodríguez-Rojo and Cocero [36] performed a first attempt to model a bed fluidized with supercritical CO2.

The number of works studying heat transfer in fluidized beds is relatively large. These studies can be divided in two main groups: those focused on the heat transfer between a solid surface and the dense bed (both fluid and particles), and those aimed to study the exchange of heat between the solid material and the fluidizing agent [37, 38]. In the latter group, the main use is for fluidized bed heat regenerators. Early studies proposed simplified mathematical models for fixed [39] and fluidized bed regenerators [40]. The use of fluidized beds as heat regenerators are also used with liquid-solid fluidized beds [41]. More recently, Shahhosseini et al. [42] experimentally analyzed the performance of a periodic fluidized bed heat exchanger and Ehsani et al. [43] numerically analyzed the effect of particle properties on a liquid-solid fluidized bed heat exchanger. Tan et al. [44] successfully substituted a plate heat exchanger by a fluidized bed heat exchanger increasing the thermal performance by $\sim$15%. Furthermore, some recent studies, mainly numerical but also experimental, have been focused on studying in detail the heat transfer mechanism in fluidized beds. Zhou et al. [45] and Al-Arkawazi [46] collected experimental data from the literature and developed thermal models that were incorporated in DEM codes. Chao et al. [47] experimentally measured the heat transfer between freely moving spheres and the dense phase of a fluidized bed and developed a model based on

4

thermal resistances. Patil et al. [48] used DEM to study heat transfer from bubble to the emulsion phase. Lichtenegger et al. [49] incorporated a heat transfer model into a recurrence DEM model which may reduce the computational cost. Lu et al. [50] added a heat transfer model to a coarse grained particle method and validated it with DEM detailed data and experimental results.

Numerical simulations of fluidized bed systems constitute a complementary tool to experiments, either to analyse variables difficult to measure in experimental units or to test extreme experimental conditions. The most common numerical techniques to simulate fluidized beds are Eulerian−Eulerian Two−Fluid Models (TFM) [51, 52, 53], Eulerian−Lagrangian approaches such as Discrete Element Models (DEM) [54, 55], or a combination of both strategies (coupled TFM−DEM) [56, 57]. The use of these techniques combined with experiments can be very effective to achieve a detailed analysis of the hydrodynamics of complex gas−solids systems [58, 59]. In the TFM approach, the gas phase and the particles or solid phase are treated as two interpenetrating continua in an Eulerian framework, using the conservation equations of fluids. The DEM strategy is based on a Lagrangian simulation of each particle trajectory coupled with an Eulerian simulation of the bulk gas flow. In the coupled TFM−DEM hybrid model, the gas and solid phases are modelled as two inter-penetrating continua as in the TFM, combined with the Lagrangian simulation of discrete particles.

The selection of the most suitable model depends on the characteristics of the system. The DEM produces a more detailed solution but at a higher computational cost, whereas the TFM needs less computational effort and the level of detail of the numerical solution is also decreased. For moderate size, lab scale units, or studies that need large simulation times, the TFM is usually a better option due to the lower computational cost. Furthermore, experimentation of supercritical fluids, such as CO_2, can entail certain difficulties because of the high temperature and pressure required, considerably reducing the number of experimental works. Therefore, the usage of numerical simulations is an excellent alternative, and possibly the unique, to study in detail fluidized systems which operate with working fluids in such conditions.

The present work performs TFM simulations of alumina based particles, commonly used for heat storage [17] as bed material, fluidized with CO_2 at high temperature and pressure conditions. The main objective is to study the technical feasibility of using beds, either in fixed or fluidized regime, as a heat recovery device in concentrating solar power plants. The bed acts as a direct contact heat exchanger between the storage material and the working fluid, CO_2 in supercritical conditions for the present study. The novelties of the work arise with the use of CO_2 in supercritical conditions, both as working fluid of the cycle and as fluidizing agent, and the comparison between fixed and fluidized bed regimes for heat recovery applications.

2. Model description

The open−source MFIX−TFM code, developed at the Energy Technology Laboratory of the US Department of Energy [60], was used to conduct the numerical simulations of a 2D bubbling fluidized bed and

a 2D fixed bed. In the MFIX−TFM code, an Eulerian–Eulerian approach is employed, considering the gas and the solid phases as Eulerian continuous phases. The 2D domain simulated represents a central plane of a cylindrical bed.

The continuum description of the gas and dense phases, i.e., Two−Fluid Model, is based on the equations of mass and momentum conservation and granular temperature balance [61]. The governing equations for the Two−Fluid Model are summarized in the following lines. The subscript s is referred to the solid phase and g to the gas phase.

Mass conservation of the gas and solid, continuum phases:

$$\frac{\partial}{\partial t}(\alpha_g \rho_g) + \nabla \cdot (\alpha_g \rho_g \vec{v_g}) = 0 \tag{1}$$

$$\frac{\partial}{\partial t}(\alpha_s \rho_s) + \nabla \cdot (\alpha_s \rho_s \vec{v_s}) = 0 \tag{2}$$

Momentum conservation of the gas and solid phases:

$$\frac{\partial}{\partial t}(\alpha_g \rho_g \vec{v_g}) + \nabla \cdot (\alpha_g \rho_g \vec{v_g} \vec{v_g}) = -\alpha_g \nabla p_g + \nabla \cdot \overline{\overline{\tau_g}} + \alpha_g \rho_g \vec{g} + K_{gs}(\vec{v_s} - \vec{v_g}) \tag{3}$$

$$\frac{\partial}{\partial t}(\alpha_s \rho_s \vec{v_s}) + \nabla \cdot (\alpha_s \rho_s \vec{v_s} \vec{v_s}) = -\alpha_s \nabla p_g - \nabla p_s + \nabla \cdot \overline{\overline{\tau_s}} + \alpha_s \rho_s \vec{g} + K_{gs}(\vec{v_g} - \vec{v_s}) \tag{4}$$

where p_i is the pressure and $\overline{\overline{\tau_i}}$ is the stress tensor for phase i.

The balance for the granular temperature, Θ, is:

$$\frac{3}{2}\left(\frac{\partial}{\partial t}(\rho_s \alpha_s \Theta) + \nabla \cdot (\rho_s \alpha_s \vec{v_s} \Theta)\right) = (-p_s \overline{\overline{I}} + \overline{\overline{\tau_s}}) : \nabla \vec{v_s} + \nabla \cdot (k_\Theta \nabla \Theta) - \gamma_\Theta - 3K_{gs}\Theta \tag{5}$$

where $(-p_s \overline{\overline{I}} + \overline{\overline{\tau_s}}) : \nabla \vec{v_s}$ is the generation of Θ by the solids stresses, $k_\Theta \nabla \Theta$ is the diffusion of Θ, γ_Θ is the collisional dissipation of Θ and $3K_{gs}\Theta$ is the transfer of random kinetic energy between the solids and the gas. In Equations 3, 4 and 5, K_{gs} is the drag force between the gas and the solid phase. The drag force correlation for the gas−solid interaction proposed by Beetstra et al. [62] was used in this work.

Conservation of internal energy for the gas phase:

$$\left(\frac{\partial (\alpha_g \rho_g c_{p,g} T_g)}{\partial t} + \nabla \cdot (\alpha_g \rho_g c_{p,g} T_g \vec{v_g})\right) = -\nabla \cdot \vec{q_g} - H_{gs} + H_{w,g}(T_w - T_g) \tag{6}$$

Energy balance for the solid phase:

$$\left(\frac{\partial (\alpha_s \rho_s c_{p,s} T_s)}{\partial t} + \nabla \cdot (\alpha_s \rho_s c_{p,s} T_s \vec{v_s})\right) = -\nabla \cdot \vec{q_s} + H_{gs} + H_{w,s}(T_w - T_s) \tag{7}$$

$\vec{q_g}$ is the gas conductive heat flux, calculated using Fourier's law:

$$\vec{q_g} = -\alpha_g k_g \nabla T_g \tag{8}$$

H_{gs} is the gas-solid interphase heat transfer:

$$H_{gs} = h_{gs}(T_g - T_s) \tag{9}$$

where h_{gs} is the convection coefficient between the gas phase and the solid phase, which can be estimated using the particle Nusselt number defined as follows:

$$Nu = \frac{d_s^2 h_{gs}}{6 k_g \alpha_s} \tag{10}$$

The correlation of Gunn [63] was used to estimate the particle Nusselt number. Buist et al. [64] carried out experiments and Direct Numerical Simulations for different gas−solid system and showed a remarkable good comparison between them and the estimations of the Gunn correlation.

$$Nu = (7 - 10\alpha_g + 5\alpha_g^2)(1 + 0.7 Re_s^{0.2} Pr^{1/3}) + (1.33 + 2.4\alpha_s + 1.2\alpha_g^2) Re_s Pr^{1/3} \tag{11}$$

with the Reynolds and Prandtl numbers as: $Re = d_s |\vec{v_s} - \vec{v_g}| \rho_g / \mu_g$ and $Pr = c_{p,g} \mu_g / k_g$.

H_w accounts for the heat transfer between the corresponding phase and the wall and $\vec{q_s}$ is the solids conductive heat flux calculated as:

$$\vec{q_s} = -\alpha_s k_s \nabla T_s \tag{12}$$

$\vec{q_s}$ accounts for the heat flux through the solids porous phase and k_s is the effective solid phase conductivity, both of which calculated following Kuipers et al. [65]. Due to the small size of the particles that conformed the bed, the Biot number is much lower than unity, which means that spatial gradients of temperature inside a particle are negligible compared to the macroscopic gradients in the bed.

2.1. Preliminary simulations of fluidization with sCO_2

For this section, a 2D bed of 0.3 m width, 0.7 m height and 0.3 m of static bed height was used with different mesh sizes to analyse the mesh sensitivity and to estimate the minimum fluidization velocity. Air and CO_2 were employed as fluidizing agents, at ambient conditions as well as conditions of high temperature ($T = 973$ K) and pressure ($p = 200$ bar). These latter conditions turn the CO_2 to supercritical conditions. Gas properties were calculated based on the database of Burcat and Ruscic [66], depending on temperature

Table 1: Simulation properties.

Bed height, H [m]	0.7
Bed width, W [m]	0.3
Static bed height, h_0 [m]	0.3
Bed material density, ρ_s [kg/m^3]	3300
Bed material diameter, d_s [μ m]	280
Coefficient of restitution, e_s [$-$]	0.9
Solids specific heat, c_{ps} [J/kgK]	1241
Solids thermal conductivity, k_s [W/mK]	4
Angle in internal friction, Φ [deg]	30

and pressure. To illustrate the variations of CO_2 properties in supercritical conditions, Figure 2 plots some normalized properties of CO_2 at 200 bar for different temperatures. Each property, π, is normalized with its maximum, π_0, for the temperature range presented. The maximum value of each property is included in the figure legend.
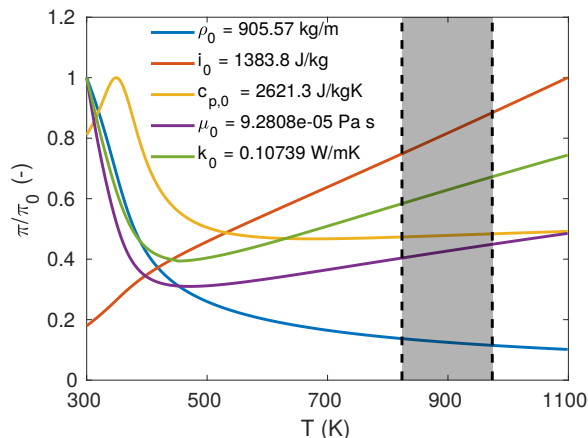

Figure 2: Variation of CO_2 properties with temperature for $p = 200$ bar. The legend shows the maximum of each property used for normalisation and the shadowed region indicates the temperature range of the present study.

Each of the simulations in this section were carried out at constant temperature to capture only the hydrodynamic effects. The solids employed as bed material posses properties similar to alumina particles, which are typically employed for heat storage [17]. Besides, particles of such characteristics have also been developed [67] and employed as direct absorption and storage media for falling particle receivers [2]. The properties of the bed and the particles used in the simulations are presented in Table 1. Particle properties match those reported by [67].

The 2D computational domain was meshed with a uniform grid and a second order accurate scheme was selected to discretise the convective derivatives of the governing equations. The gas flow is fed uniformly

through the bottom of the bed using a velocity inlet boundary condition. The gas flow leaves the system through the top boundary at a constant pressure. A no-slip boundary condition is used for the gas and continuum solid phases at the side walls of the bed. Previous works have demonstrated that the lateral boundary condition does not have a strong effect in this kind of simulations [68, 69]. In the simulations of this section, both the particles and the gas are at the same temperature, the bed is assumed to be well isolated, which means that the walls are considered adiabatic and, therefore, these simulations are isothermal. To increase the accuracy of the simulations, the balance for the granular temperature is solved using the partial differential equation (Equation 5) instead of a simplified algebraic equation.

2.1.1. Mesh sensitivity

The first part of the results is focused on the mesh sensitivity analysis. Fluidization using CO_2 in supercritical conditions (sCO_2) may differ from the classical gas−solid fluidization. Therefore, typical mesh sizes for gas−solid systems encountered in the literature should be taken with caution in the present case. Li et al. [68] and Hernández-Jiménez et al. [69] concluded that a mesh of 5 mm length is appropriate to simulate gas−solid fluidized beds with similar characteristics to those of the present work, except for the supercritical condition of the fluidizing agent.

Figure 3 represents some instantaneous snapshots of the solids volume fraction, α_s, for different meshes of square cell size with $\Delta s = 5$, 4, 3, 2.5 and 2 mm in length. The cases simulated were run at a temperature $T = 898$ K and a pressure of $p = 200$ bar, which are conditions similar to those analysed in Section 3 (same pressure and average temperature) and the superficial gas velocity, U_0, is 0.07 m/s. Figure 3 shows that the structures appearing in the bed differ from the classical rounded bubbles found in gas−solid bubbling fluidized beds. This can be mainly attributed to the increase of density of the gas at such conditions, which increases two orders of magnitude from ambient conditions. In view of Figure 3, a mesh of 5 mm size is not fine enough to solve the aforementioned structures, as well as the mesh of 4 mm. Nonetheless, a more quantitative analysis is required to shed light into the differences obtained between the meshes of 3 mm, 2.5 mm and 2 mm.

Figure 4 shows the time averaged bubble fraction of the bed, δ_b, as a function of the different mesh sizes tested. Data is extracted every 0.05 s during 20 s and the start-up is eliminated to calculate the time−averaged value. The bubble fraction, δ_b, represents the fraction of the total frontal area occupied by bubbles at each time instant divided by the initial frontal area of the bed. A bubble is defined as the area delimited with a value of $\alpha_s = 0.3$. Therefore, δ_b is calculated at each time instant and the time average of δ_b is performed subsequently. It is clear from Figure 4 that, in terms of δ_b, a mesh of 2.5 mm have reached mesh independence since the time averaged δ_b is almost the same for the 2.5 (30404 nodes) and 2 mm (53504 nodes) meshes. The mesh size selected hereafter is 2.5 mm for all the cases.
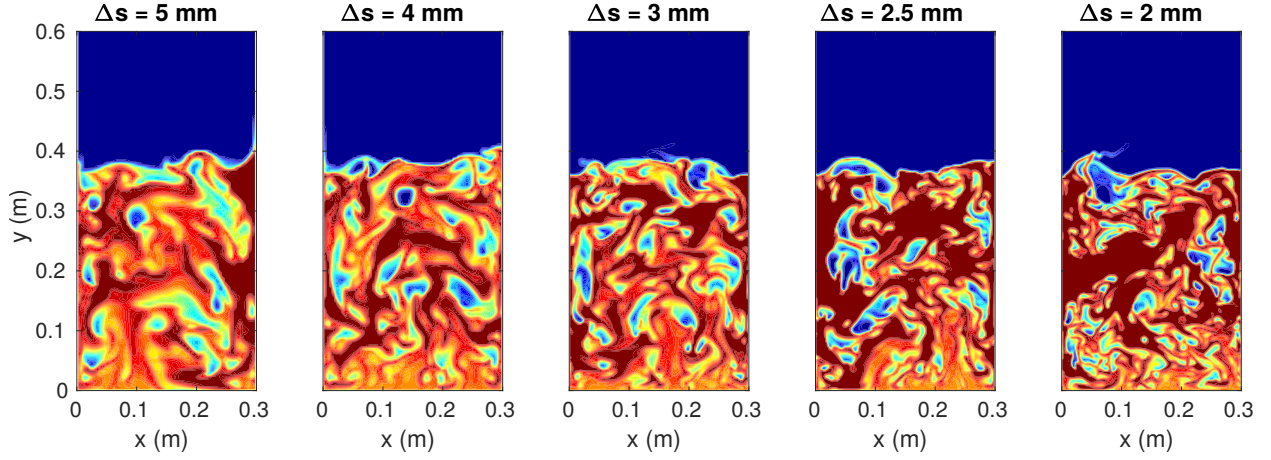
Figure 3: Instantaneous snapshots of the solids volume fraction, α_s, for different mesh sizes. Fluidization with sCO$_2$ at $U_0 = 0.07$ m/s, $T = 898$ K, $p = 200$ bar.
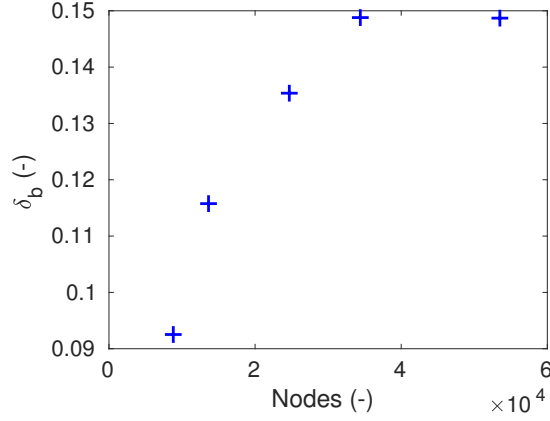

Figure 4: Time averaged bubble fraction, δ_b, for different mesh sizes.

2.1.2. Minimum fluidization velocity estimation under high temperature and pressure

This subsection focuses on the estimation of the minimum fluidization velocity, U_{mf}, under ambient conditions and conditions of high temperature ($T = 973$ K) and pressure ($p = 200$ bar), using the parameters of Table 1. The calculation of U_{mf} from the Two-Fluid Model is important for two reasons; firstly to check if the model matches the estimations from classical correlations and, secondly, to clearly distinguish fixed and fluidized bed regimes to properly accomplish the subsequent analysis. The temperature selected to estimate U_{mf} is the maximum temperature of the problem analysed (see Section 3). In general, U_{mf} decreases with temperature. Thus, if U_{mf} were determined at a lower temperature than the maximum, the bed would be fluidized even at values $U_0/U_{mf} < 1$ if the gas temperature increases sufficiently in the bed. The fluidizing agents studied are air and CO$_2$. The aim of using air and CO$_2$ at different conditions is to perform a practical validation of U_{mf} with classical correlations found in the literature. Air at ambient conditions is

10

included in the comparison because correlations and simulation models have been developed and tested in such conditions. Hence, they can give an idea of the deviation between the simulation and the correlations for U_{mf}. The effect of pressure and temperature is considered in these correlations through the variation of density and viscosity of the fluidizing agent. The correlations used for the validation are those proposed by Ergun [70], Wen & Yu (W-Y) [71], Carman−Kozeny (C-K) [72] and Grace [73]. The method of the mean pressure was employed to estimate U_{mf} using the simulations results for different gas velocities within a range from 1 cm/s to 15 cm/s.
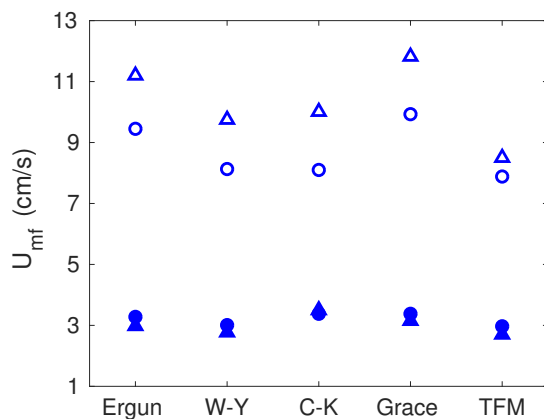

Figure 5: Minimum fluidization velocity, U_{mf}, estimation with different correlations and predicted by TFM simulations. Empty symbols represents ambient conditions and filled symbols $T = 973$ K and $p = 200$ bar. $\bigcirc$ is used for air and $\triangle$ for CO_2.

Figure 5 shows the minimum fluidization velocity estimation, U_{mf}, obtained form different correlations and predicted by the simulations. The differences between the different correlations are small, within ± 1 cm/s at ambient conditions and ± 0.5 cm/s at high temperature and high pressure. The differences that the TFM prediction presents regarding any of the correlations is of the same order. Differences between ambient conditions and high pressure and temperature conditions can be also observed on Figure 5. The increase of density and viscosity when increasing both temperature and pressure promotes a reduction of the apparent minimum fluidization velocity. The values of U_{mf} for air and CO_2 are greater at ambient conditions, whereas these estimations of U_{mf} are closer at high temperature and pressure. In general, dispersion of results of U_{mf} is smaller at high temperature and pressure than at ambient conditions. Therefore, the estimation of U_{mf} obtained from the simulations, which resulted in 2.7 cm/s for supercritical CO_2, will be used as base for the subsequent simulations.

3. Fixed and fluidized bed for heat recovery in concentrating solar power plants

Fixed or fluidized beds can be used as a direct contact heat exchanger between the particles and the working fluid of a CSP tower, which is CO_2 in supercritical conditions in this study (Figure 1). These

particles can constitute only the storage media of the CSP tower, or the material that captures the energy in a particle receiver if the receiver−storage assembly were pressurized [17, 23]. Direct contact reduces the time response and improves the heat transfer efficiency from the solid particles to the heat transfer fluid, while maintaining the stream exergy of the fluid to enhance the overall power cycle efficiency. Several bed configurations were simulated to derive the best configuration that enhances heat transfer both from the energetic and the exergetic points of view. In particular, these simulations can help to analyse the technical feasibility of using either a fluidized bed or a fixed bed for heat recovery applications using supercritical CO_2 as working fluid.

Table 2 summarizes the bed configurations simulated. The simulation parameters are specified in Section 2.1. The 2D simulation is a simplification of a cylindrical 3D bed with the 2D width representing the 3D bed diameter ($W = D_{bed}$). Li [74] developed a simplified 2.5D model to simulate 3D cylindrical beds without the need of considering the full domain. Despite the good prediction of the 2.5D model, he also highlighted that the 2D simulation yielded good qualitative and reasonable quantitative agreement to experimental measurements of 3D beds. The mass flow rate of sCO_2 and the mass of particles reported in Table 2 are then those of considering a cylindrical 3D bed of diameter and gas superficial velocity equal to the width and gas velocity of the simulated 2D bed, respectively. As in the previous section, the bed is assumed to be well isolated which means that the walls are considered adiabatic. Johnson et al. [16] considered heat losses through the external walls to the ambient in a similar system resulting in approximately 4% of the thermal power supplied by the storage system to the turbine. Under the assumption that the dominant thermal resistance is due to conduction in the bed walls, heat losses would have similar effects on both beds. Thus, consideration of heat losses through the walls would reduce the efficiency of both systems similarly too. In all cases, the initial temperature of both the gas and bed material is 973 K and the sCO_2 is supplied at a temperature of 823 K at the bottom of the bed. Assuming a uniform initial temperature of the particles of 973 K means that the charging process, either using particles directly heated in the solar receiver or indirectly heated by a working fluid, has been totally completed. Only totally charged beds will be considered in the present work, so the analysis can be focused on the discharging process. This temperature difference, from 823 K to 973 K, represents typical conditions of the sCO_2 between the heat recovery unit and the turbine of a Brayton cycle [7, 75, 76, 77], see Figure 1.

The different configurations of Table 2 used the same amount of bed material. This amount represents the mass of particles in the storage tank. In the case that the particles come directly from a particle receiver, it represents the mass of particles that the receiver is capable of heating up in each filling of the storage tank. Ho [2] reported mass flow rates ranging from 1 to 7 kg/s for the heated particles in a tested particle receiver of ∼1 MW_t. Besides, Besarati and Goswami [75] estimated values around 3 kg/s of mass flow rate supplied to CO_2 for turbines of approximately 300 kW.

Table 2: Fixed and fluidized bed configurations.

Configuration	1	2	3	4	5
Bed width, $W = D_{bed}$ [m]	0.3	0.49	0.39	0.6	0.3
Static bed height, h_0 [m]	0.3	0.1125	0.1775	0.075	0.3
Gas velocity, U_0 [cm/s]	5.4	2.02			
CO_2 mass flow, $\dot{m}_{CO_2}$ [kg/s]	0.477	0.477	0.302	0.716	0.162
Mass of solid particles, m_s [kg]	41.98				
Fluidization velocity, U_0/U_{mf} [-]	2	0.75			
Regime	Fluidized	Fixed			

3.1. Fixed and fluidized bed comparison

Configurations 1 and 2 aimed to compare the fixed and fluidized regimes, maintaining the mass flow rate of CO_2 constant. While in Configuration 1 the bed is narrower so that the bed material is more confined and reaches a higher bed height, in Configuration 2 the bed material is more spread in a wider bed and the superficial gas velocity for the sCO_2 is smaller than in Configuration 1 for the same mass flow rate. This decrease of superficial gas velocity causes the change from fluidized bed conditions in Configuration 1 to fixed bed conditions in Configuration 2. Furthermore, the purpose of Configurations 3 and 4 is to compare the effect of changing the mass flow rate of sCO_2 under fixed bed conditions by rearranging the bed material while maintaining the same sCO_2 velocity as Configuration 2, i.e., preserving the fixed bed configuration.

The effect of the fixed and fluidized bed configurations on the heat transfer from particles to the sCO_2 was analysed by simulating Configurations 1 and 2 for 300 s of physical time. Figure 6 shows the time evolution of the gas temperature, T_{CO_2}, obtained in the simulation. The map represents the temperature, averaged over the horizontal dimension, plotted as a function of the distance to the distributor, y, and time, t. Both gas and solids are nearly in local thermal equilibrium in the bed, therefore gas temperature resembles also solids temperature. In Figure 6a, the results for the fixed bed are presented, The solids are progressively cooled with time, whereas gas is heated while percolating through the layer of solids. An average gas temperature of $T_{CO_2} = 973$ K is achieved at the exit of the bed during around 70 s until the decrease of solids temperature reaches the top of the fixed bed. Then, T_{CO_2} decreases suddenly due to the decrease of the temperature of the solids in the whole bed. This means that the gas is extracted at the maximum temperature available during approximately 70 s for a fixed bed. Figure 6b shows the results for the fluidized regime. In this case, the temperature is almost uniform along the bed height, reflecting the condition of perfect mixing of the fluidized bed. Due to this perfect mixing, the exit temperature of the sCO_2 decreases progressively from the beginning of the simulation. Also, the higher gas velocity of the fluidized bed results in a higher heat transfer from the particles to the fluid.

Figure 7 shows the time evolution of the gas temperature, T_{CO_2}, horizontally averaged at the exit, for the
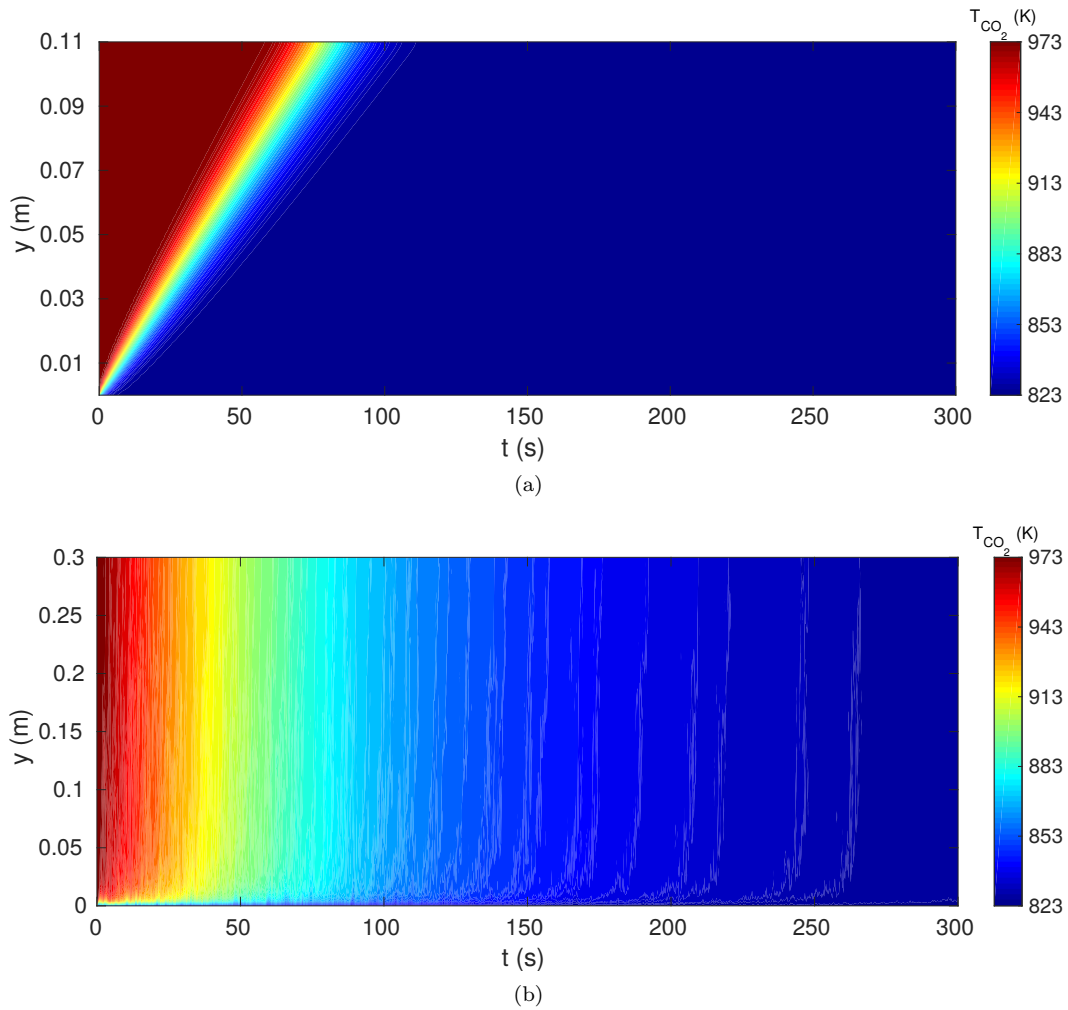
Figure 6: Contour map of the CO_2 temperature, T_{co_2}, horizontally averaged, as a function of height, y, and time, t, for the fixed bed (a) and fluidized (b) conditions. Configurations 1 and 2.

fixed and fluidized bed heat exchangers (Configurations 1 and 2 of Table 2). This temperature is extracted at ~ 5 cm above the surface of the bed in each case. Remarkable differences for the outlet gas temperature of a fixed and fluidized bed heat exchanger can be observed in the figure. The fixed bed heat exchanger keeps a higher outlet gas temperature during a much longer time than the fluidized bed. In fact, the fluidized case shows an inverse exponential decrease of the gas temperature at the outlet, which is in agreement with a basic energy balance of the system, in which all the solids reduce their temperature at a rate proportional to the difference between the solids temperature the inlet gas temperature.

The heat rate, $\dot{Q}_s$, dissipated from the solids to the sCO$_2$, and the heat rate absorbed by the sCO$_2$, $\dot{Q}_{CO_2}$, occur in a control volume that encloses the bed. $\dot{Q}_s$ and $\dot{Q}_{CO_2}$ must be equal for an externally adiabatic heat exchanger. For the fluidized bed regime, the temperature of solids, T_s can be considered uniform in all the bed. The sCO$_2$ is assumed to behave, as a first approximation, as an ideal gas with constant specific
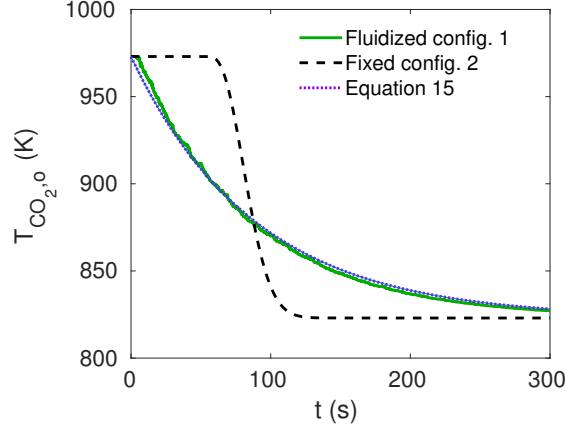
14

Figure 7: Outlet gas temperature, T_{CO_2}, horizontally averaged, as a function time, t, for the fixed bed and fluidized conditions.

heats. This assumption is valid since the compressibility factor for the CO_2 in the range studied is close to 1 and the specific heat is almost constant (Figure 2). Then, $\dot{Q}_s$ and $\dot{Q}_{CO_2}$ can be calculated as:

$$\dot{Q}_s = -m_s c_{p,s} \frac{dT_s}{dt} \tag{13}$$

$$\dot{Q}_{CO_2} = \dot{m}_{CO_2} c_{p,CO_2} (T_{CO_2,o}(t) - T_{CO_2,i}) + M_{co_2} c_{p,CO_2} \frac{dT_{co_2}}{dt} \tag{14}$$

where $T_{CO_2,o}$ and $T_{CO_2,i}$ represent the temperature at the outlet and inlet of the fluidized bed heat exchanger, respectively. M_{co_2} and dT_{co_2}/dt represent the mass and temperature variation with time of the CO_2 in the control volume. $T_{CO_2,i}$ is constant because the sCO_2 is entering the system always at the same temperature, 823 K in the present study. The small variations of the fluid properties with temperature (density and specific heat) are neglected in Equation 14 for simplicity. The assumption of perfect mixing in the fluidized bed means that all the solids are at the same temperature at each time instant, thus T_s depends only on time for the fluidized bed heat exchanger. Thermal equilibrium of the gas and solids can be also assumed for the fluidized bed heat exchanger due to the high heat transfer area and local convection heat transfer coefficient. Therefore the temperature at the outlet of the sCO_2 is considered equal to the temperature of the solids at each time instant, $T_{CO_2,o} = T_s$, as well as the temperature of the CO_2 in the control volume, $T_{CO_2} = T_s$. Finally, the lumped capacitance approach can be applied to solve the differential Equations 13 and 14, for small solid particles for which the Biot number is low. The following expression is obtained for the time evolution of the temperature of the sCO_2 at the outlet:

$$T_s(t) = T_{CO_2,o}(t) = \exp(-t/\tau)(T_{s,i} - T_{CO_2,i}) + T_{CO_2,i} \tag{15}$$

15

where $T_{s,i}$ is the initial solids temperature (973 K) and τ is the characteristic thermal time of the problem:

$$\tau = \frac{m_s c_{p,s} + m_{CO_2,cv} c_{p,CO_2}}{\dot{m}_{CO_2} c_{p,CO_2}} \tag{16}$$

The results obtained from Equation 15 are also included in Figure 7. Note that the small differences are due to the fact that Equation 15 has been calculated assuming constant properties for the sCO_2 at a temperature of 898 K and that the outlet gas temperature has been sampled slightly above the surface of the bed. Looking at Equations 15 and 16, the time evolution of the outlet temperature of the fluidized bed heat exchanger will be identical provided that the working conditions of mass flow rate of sCO_2, temperature difference, and mass of heated particles remain constant.

The capability of the sCO_2 flow leaving the heat exchanger to generate mechanical power in a thermodynamic cycle depends on the outlet temperature. Therefore, a simple way to characterise this capability is employing the Carnot efficiency using the outlet temperature of the sCO_2 as the hot reservoir and assuming the cold reservoir at a temperature slightly above ambient temperature ($T_c = 313$ K). The time evolution of η_{Carnot} is shown in Figure 8a.

$$\eta_{Carnot} = 1 - \frac{T_c}{T_{CO_2,o}} \tag{17}$$

Furthermore, characterisation of the capability of the fixed and fluidized heat exchangers to generate mechanical power can be done in more detail in terms of exergy or availability. In thermodynamics, the exergy or availability of a system is the maximum useful work possible during a process that brings the system into equilibrium with a heat reservoir. This means that exergy is the energy available to be transformed into work. The capability to generate mechanical power is obtained by calculating the increase in the availability of the sCO_2 flow circulating through each heat exchanger. Combining the first and second laws of thermodynamics [78], an availability balance for a control volume can be postulated and the availability change between the inlet and the outlet in the heat exchanger can be expressed as:

$$\Delta\dot{A} = \dot{m}_o a_o - \dot{m}_i a_i \tag{18}$$

where $\Delta a = a_o - a_i = (i_o - i_i) - T_0(s_o - s_i) + (c_o^2 - c_i^2)/2 + (z_o - z_i)g$, with i and s the enthalpy and entropy of the fluid, respectively. T_0 is the temperature of a reference state which has been selected here as the sCO_2 inlet conditions. The variations of kinetic and potential energy between the inlet ant the outlet of the exchanger can be neglected and the variations of enthalpy and entropy can be estimated using the ideal

gas model with constant specific heats (see Figure 2:

$$i_o - i_i = c_p(T_o - T_i) \tag{19}$$

$$s_o - s_i = c_p \ln \frac{T_o}{T_i} - c_p \frac{\gamma - 1}{\gamma} \ln \frac{p_o}{p_i} \tag{20}$$

where γ is the ratio of specific heats. Using Equations 19, 20 and 21, $\Delta \dot{A}$ can be calculated just as a function of the temperature increase and pressure drop:

$$\Delta \dot{A} = \dot{m}_{CO_2} c_{p,CO_2} \left[(T_{CO_2,o} - T_{CO_2,i}) - T_{CO_2,i} \left(\ln \left(\frac{T_{CO_2,o}}{T_{CO_2,i}} \right) - \frac{\gamma - 1}{\gamma} \ln \left(\frac{p_{CO_2,o} - \Delta p_{CO_2}}{p_{CO_2,i}} \right) \right) \right] \tag{21}$$

where $p_{CO_2,i}$ is the pressure of the sCO$_2$ at the inlet of the heat exchanger (200 bar in the present study) and Δp_{CO_2} is the pressure drop through the bed and the distributor. A distributor with a pressure drop of 30% the pressure drop due to the weight of the particles ($\Delta p_{CO_2} = \rho_s g h_0 \alpha_s$) at U_{mf} conditions is considered as a typical design point [79], and the pressure drop of the bed is extracted at each time of the simulation. The pressure drop through the distributor should be calculated considering the temperature of the fluidizing agent, as stated by Sánchez-Prieto et al. [80]. The same design condition is used for the fixed and fluidized bed for simplicity and to make the comparison consistent. The design condition of the 30% bed pressure drop is applied at minimum fluidization conditions and then the pressure drop through the distributor is calculated for each bed with its corresponding superficial gas velocity. The results of the increase in availability of the sCO$_2$ flow can be found in Figure 8b, which shows the time evolution of $\Delta \dot{A}$.
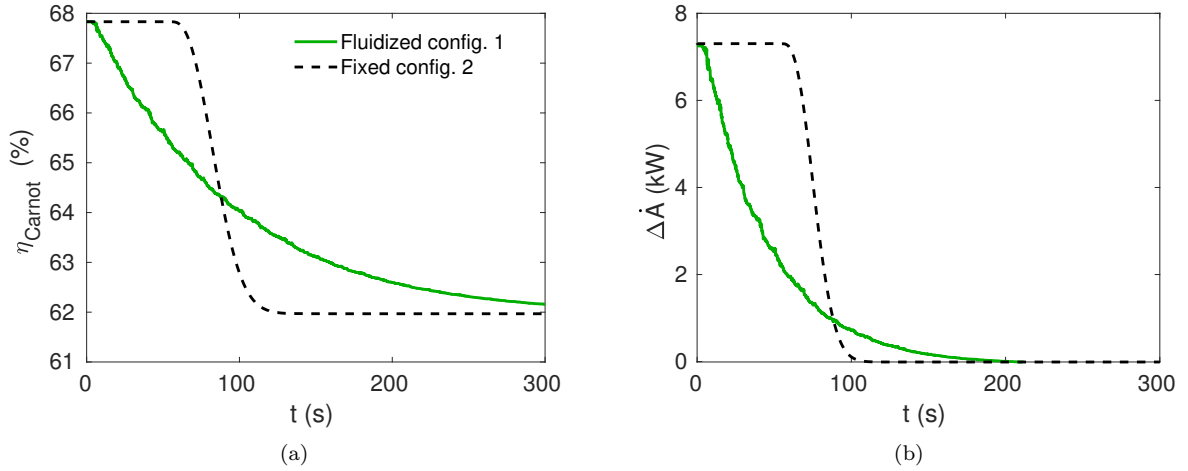

Figure 8: Time evolution of the Carnot efficiency (a) and increase of availability of the sCO$_2$ between the inlet and the outlet, $\Delta \dot{A}$, (b) for the fixed and fluidized bed heat exchangers.

Carnot efficiency as well as the increase in availability of the gas when the bed is operated under fixed

17

conditions is maximum during the time interval in which the outlet temperature is maximum. Then, η_{Carnot} and $\Delta\dot{A}$ for the fixed bed heat exchanger suddenly decrease also at a rate proportional to this temperature. In the case of the fluidized bed, η_{Carnot} and $\Delta\dot{A}$ decrease exponentially following the same trend as the average temperature of the solids in the bed. In view of Figure 8, the the effect of differences in pressure drop in the fixed and fluidized bed heat exchangers is negligible, i.e. the trend of the Carnot efficiency, which depends only on the temperature, is the almost the same than $\Delta\dot{A}$. The effect of the pressure drop can be appreciated only during the first time instants, where $\Delta\dot{A}$ is maximum in both cases and the maximum of $\Delta\dot{A}$ for the fluidized is lower than for the fixed bed due to the higher pressure drop. Then, the major contribution to the change in $\Delta\dot{A}$ is because the gas temperature variation.

Following Johnson et al. [16], the fractional exergetic efficiency can be calculated to further compare the fixed and fluidized beds. The fractional exergetic efficiency represents the exergy recovered by the system over the exergy that could be recovered from a perfect thermal reservoir from $t_{ini} = 0$ s to the final time t_{fin}:

$$\eta_{Ex} = \frac{\int_{t_{ini}}^{t_{fin}} \left[(T_{CO_2,o} - T_{CO_2,i}) - T_{CO_2,o} \ln \frac{T_{CO_2,o}}{T_{CO_2,i}} \right] dt}{\left[(T_{s,i} - T_{CO_2,i}) - T_{CO_2,o} \ln \frac{T_{s,i}}{T_{CO_2,i}} \right] \Delta t_{rec}} \tag{22}$$

where $\Delta t_{rec} = t_{fin} - t_{ini}$ is the recovery time interval. The results of applying Equation 22 to the simulation data are given in Figure 9, where η_{Ex} was calculated using the inlet temperature of the CO_2 as reference, similarly to Equation 21. Instead of a single value, the time evolution of η_{Ex} is represented for the time interval analysed, Δt_{rec}. According to the definition, η_{Ex} strongly depends on the storage/recovery time. As Figure 9 reflects, η_{Ex} behaves similarly to η_{Carnot} and $\Delta\dot{A}$, indicating that the fixed bed heat exchanger enables to reach the maximum value possible of η_{Ex} during longer times than the fluidized bed heat exchanger. Furthermore, Figure 9 shows also that the fractional exergetic efficiency is higher for the fixed bed than for the fluidized bed for the whole time evolution. This is so because η_{Ex} is a cumulative magnitude of the area below the curves of Figure 8b and the fixed bed has higher values of $\Delta\dot{A}$ in shorter times than the fluidized bed. In contrast to the results shown in Figure 8b, where $\Delta\dot{A}$ becomes higher for the fluidized bed at larger times.

However, pressure drop in the bed can influence the parasitic pumping consumption of the plant. Therefore, it is important to quantify its effect separately from the increase of availability. The mean value of the pressure drop, including the pressure drop of the distributor, is 13.73 kPa and 3.01 kPa for the fluidized and fixed bed, respectively. In the fluidized bed case, the particles are fully supported by the gas as the superficial gas velocity, U_0, corresponds to a velocity higher than the minimum fluidization velocity, U_{mf}, whereas in the fixed bed case $U_0 < U_{mf}$, which means that the particles are partially supported by the gas.
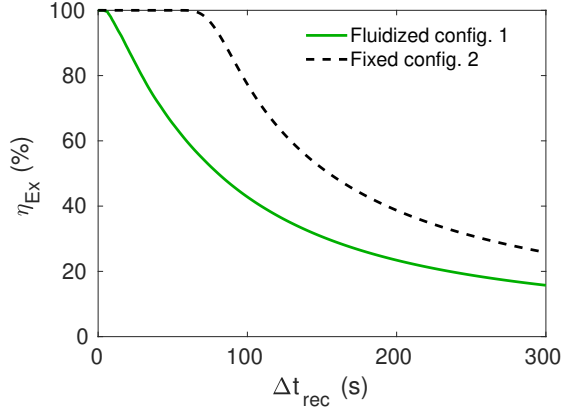
Figure 9: Time evolution of the fractional exergetic efficiency, η_{Ex}, for the fixed and fluidized bed heat exchangers.

In the fluidized bed case, the pressure drop is basically the weight of the particles and the gas in addition to the pressure drop of the distributor. In the fixed bed case, the main contribution is the pressure drop of the distributor since the bed is below the fluidization regime and the bulk of the particles is not suspended by the fluidizing agent. Then, the overall value of Δp is lower in the fixed bed case because the gas velocities are lower and the design point is the same as in the fluidized bed case. In absolute terms, the pressure drop differences between the fixed and fluidized bed can be considered negligible since the sCO_2 leaves the beds at a pressure of 200 bar. Nonetheless, in relative terms, the fluidized bed case presents a pressure drop of around 4 times the pressure drop of the fixed bed.

Figure 10a shows the average solids temperature, $\overline{T_s}$, which is T_s spatially averaged in the whole bed at each time instant. The decrease of average solids temperature is faster in the fixed bed than in the fluidized bed heat exchanger. Therefore, the recovery time to heat up the solid particles of the storage system again for the next operation cycle can be done earlier in the fixed bed while much longer times are required in the fluidized bed. For example, ~ 100 s are required for the fixed bed to reach a $\sim 95\%$ of the asymptotic temperature whereas ~ 150 s are needed in the case of the fluidized bed heat exchanger. Figure 10b depicts the total energy, E, absorbed by the sCO_2, calculated as the energy released from the solids to the sCO_2, which is determined considering the averaged solids temperature in the whole bed, $\overline{T_s}$:

$$E = -m_s c_{ps}(\overline{T_s} - T_{s,i}) \tag{23}$$

During the first time instants, the evolution of the energy, E, is almost the same for both configurations, however the rate of energy absorbed by the gas, dE/dt, in the case of the fluidized bed heat exchanger is progressively reduced while the outlet temperature of the sCO_2 decreases. In contrast, the rate of the energy absorbed by the sCO_2 in the fixed bed heat exchanger is constant during the time period for which the outlet temperature of sCO_2 is maximum and, after this period, the energy absorbed rate is reduced drastically.
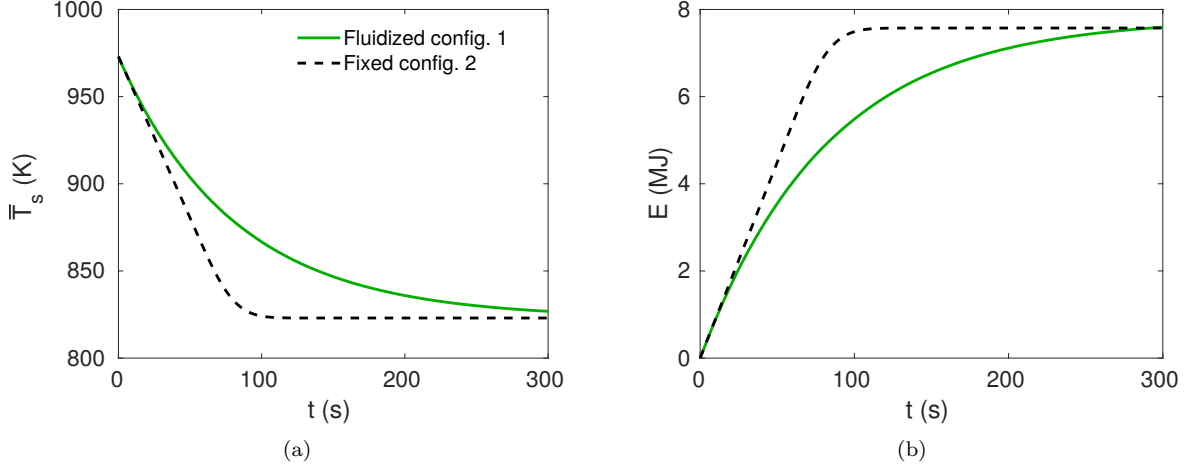
19

Figure 10: Time evolution of the average solids temperature, $\overline{T_s}$ (a) and the total energy absorbed by the gas, E, (b), for the bed under fixed and fluidized conditions.

Notice also that both curves tend to the same value of $E(t \to \infty)$, which corresponds to the initial thermal energy contained in the bed particles relative to the gas inlet temperature $E = m_s c_{p,s}(T_{s,i} - T_{CO_2,i})$. However the fixed bed heat exchanger reaches this value much faster than the fluidized bed exchanger.

3.2. Fixed bed parametric study

From the above analysis, the optimal configuration for the heat recovery application proposed is that of fixed bed, for the same working conditions in the fixed and fluidized beds, i.e., same mass flow rate of sCO_2, temperature difference, and mass of heated particles. During a short period of time, the fixed bed configuration of the heat exchanger permits the reduction of the average solids temperature while maintaining a maximum outlet temperature for the sCO_2 flow, i.e., maximizing the availability of the flow to generate mechanical power (Figure 8). Therefore, the discharge of energy from the solid particles to the sCO_2 is much more efficient under fixed conditions and thus the energy absorption by the sCO_2 is also faster (Figure 10b). Therefore, a comparison of fixed bed regime under different conditions (Table 2) can be performed to find the effect of varying the sCO_2 mass flow rate on the behaviour of the system (Configurations 2, 3 and 4).

Figure 11 shows the outlet gas temperature, $T_{CO_2,o}$, horizontally averaged, the increase of availability of the sCO_2 in the heat exchangers, $\Delta\dot{A}$; the average solids temperature, $\overline{T_s}$, and the total energy, E, absorbed by the sCO_2 for the different configurations of the fixed bed as a function of time (Table 2). An increase of the mass flow rate of sCO_2, $\dot{m}_{CO_2}$, reduces the time period for which the outlet temperature of sCO_2 is maximum. The energy absorbed by the sCO_2 approaches its maximum value sooner with an increase of $\dot{m}_{CO_2}$. Furthermore, the increase of the availability also starts to diminish earlier from its maximum value for higher sCO_2 mass flow rates, but this maximum value is greater since it is directly proportional to $\dot{m}_{CO_2}$

(Equation 21). Therefore, counteracting effects are present when analysing $\Delta \dot{A}$. Increasing $\dot{m}_{CO_2}$ increases also the maximum value of $\Delta \dot{A}$ but, in contrast, this maximum is maintained during a shorter period of time. Both the reduction of the average solids temperature and the increase of the energy absorbed are accelerated when the mass flow rate of sCO_2 is increased. The solids are cooled faster and, therefore, the energy released by the solids is absorbed by the sCO_2 sooner.
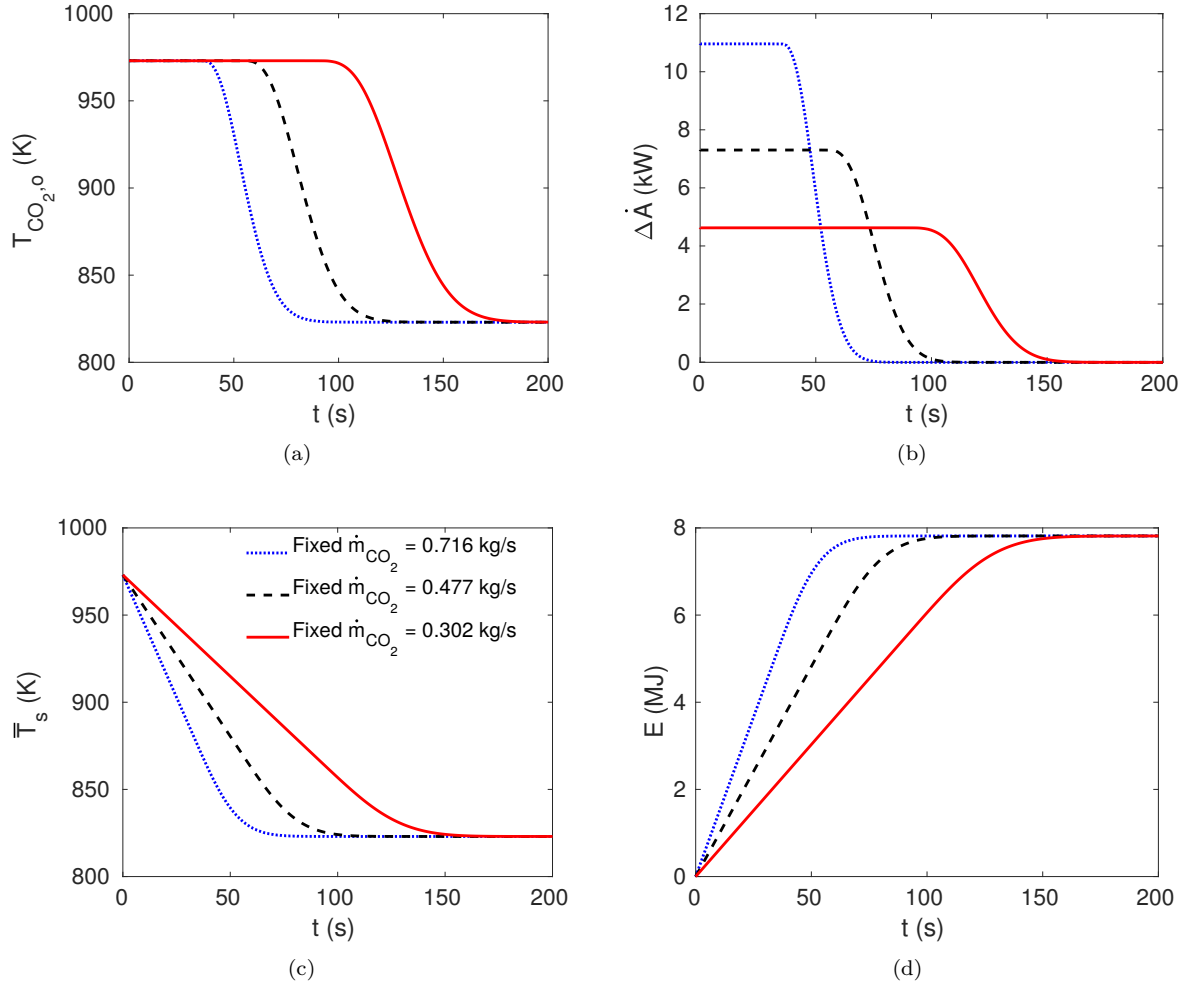

Figure 11: Time evolution of the outlet gas temperature, T_g, (a), increase of availability of the gas, $\Delta \dot{A}$, (b), average solids temperature, $\overline{T_s}$, (c) and the total energy accumulated by the gas, E, (d), for the different configurations of fixed bed.

For a real application, the selection of the sCO_2 mass flow rate should be based on the capability of the plant to heat up the solid particles of the storage system. These solids of the fixed bed heat exchanger should be reheated once the sCO_2 outlet temperature starts to decrease, which is when the solids temperature at the top of the bed tends to the inlet temperature of the sCO_2. This recovery time, t_r, can be estimated as the time when the increase of availability of gas, $\Delta \dot{A}$, starts to decrease. Figure 11b shows that the mass flow rate is inverse proportional to the recovery time. t_r is obtained here as the time needed to reach the

95% of the maximum value of $\Delta\dot{A}$. A curve fitting can be performed to relate $\dot{m}_{CO_2}$ and t_r obtained in the simulation. Given a recovery time, $\dot{m}_{CO_2}$ can be obtained from the curve fitting and the diameter of the heat exchanger can be calculated as:

$$D_{bed} = \sqrt{\frac{4}{\pi} \frac{\dot{m}_{CO_2}}{\rho_{CO_2} \frac{U}{U_{mf}} U_{mf}}} \tag{24}$$

A fixed bed regime must be ensured in Equation 24, i.e., $U_0 < U_{mf}$, since this is the optimal configuration for the heat recovery application analysed in terms of the outlet sCO$_2$ flow availability.

The calculation procedure described above is summarised in Figure 12, where the curve fitting to relate $\dot{m}_{CO_2}$ and t_r is combined with the calculation of the bed diameter using Equation 24. The points used to obtain the fitting, which are extracted from the simulation results of Configurations 2, 3, 4 and 5, are also included in the figure. As commented before, these points correspond to the time needed to reach the 95% of the maximum value of $\Delta\dot{A}$ for each $\dot{m}_{CO_2}$ in the cases simulated. It is worth to mention that the recovery times obtained could be augmented by increasing the mass of heated particles. These particles could be placed in several beds working in sequential or in parallel mode.
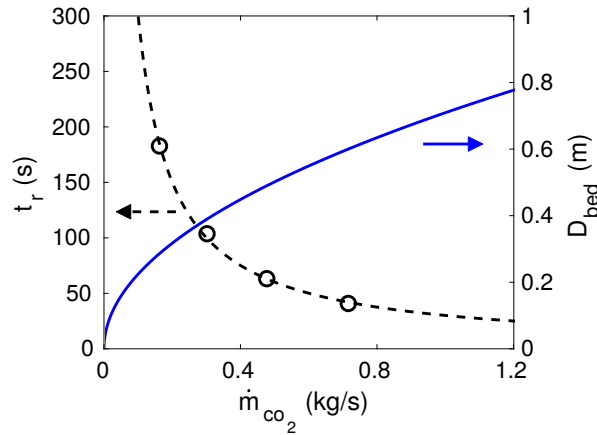
Figure 12: Recovery time, t_r and diameter on the fixed bed heat exchanger, D_{bed} as a function of the mass flow rate of sCO2, $\dot{m}_{CO_2}$ for the fixed bed conditions analysed.

4. Conclusions

In the present work, numerical simulations using the Two Fluid Model have been carried out to study the fluidization when using supercritical CO$_2$ as fluidizing agent for heat recovery applications. The main goal is to increase the efficiency of the heat recovery of CSP applications where energy is stored as sensible heat in a granular material. This granular material can be just the material of a thermal storage tank but also the particles coming from a falling particle receiver.

The technical feasibility of using either a fluidized bed or a fixed bed as direct contact heat exchanger has been analysed. The analysis has been performed based on the temperature of solids, the temperature of the CO_2 at the outlet of the heat exchanger and the resulting increase in energy and availability of the CO_2 stream. The simulation results show that fixed bed leads to an increase of the CO_2 availability during longer time compared to fluidized bed. Since the objective of the present study is the exergy recovery of heat from the solids to the working fluid, a fixed bed heat exchanger is more suitable than a fluidized bed. As a result, different fixed bed configurations have been analysed in this work to analyse the heat recovery time.

Nomenclature

A	Availability [J]
a_i	Specific availability of the fluid at the inlet of the control volume [J/kg]
a_o	Specific availability of the fluid at the outlet of the control volume [J/kg]
$c_i^2/2$	Specific kinetic energy at the inlet [J/kg]
$c_o^2/2$	Specific kinetic energy at the outlet [J/kg]
$c_{p,g}$	Gas specific heat at constant pressure [J/kgK]
$c_{p,s}$	Solids specific heat [J/kgK]
c_p	Specific heat at constant pressure [J/kgK]
D_b	Bubble diameter [m]
D_{bed}	Bed diameter [m]
d_s	Dense phase particle diameter [m]
E	Total energy absorbed by the CO_2 [J]
e_s	Coefficient of restitution [$-$]
$\vec{g}$	Gravity [m^2/s]
H	Bed height [m]
H_w	Heat transfer coefficient between each phase and the wall [W/K]

H_{gs}	Gas−solid interphase heat transfer [W]
h_0	Static bed height [m]
h_{gs}	Convection coefficient between gas and solid phase [W/K]
$\overline{\overline{I}}$	Unity matrix [−]
i_i	Specific enthalpy at the inlet [J/kg]
i_o	Specific enthalpy at the outlet [J/kg]
K_{gs}	Drag force between gas and solids [kg/m³s]
k_g	Gas conductivity [W/mK]
k_Θ	Diffusion coefficient for granular energy [kg/ms]
k_s	Effective solid phase conductivity [W/mK]
$\dot{m}_g$	Mass flow rate of gas [kg/s]
$\dot{m}_{CO_2}$	Mass flow rate of CO_2 [kg/s]
m_s	Mass of solid particles [kg]
M_{CO_2}	Mass of CO_2 in the control volume [kg]
Nu	Nusselt number [−]
Nodes	Number of computational nodes [−]
Pr	Prandtl number [−]
p	Pressure [Pa]
p_g	Gas pressure [Pa]
p_i	Inlet pressure [Pa]
p_o	Outlet pressure [Pa]
p_s	Solids pressure [Pa]
$p_{CO_2,i}$	Inlet pressure of the CO_2 [Pa]
$p_{CO_2,o}$	Outlet pressure of the CO_2 [Pa]

$\dot{Q}_s$	Heat transfer rate dissipated from the solids [W]
$\dot{Q}_{CO_2}$	Heat transfer rate absorbed by the CO_2 [W]
$\vec{q}_g$	Gas conductive heat flux [W]
$\vec{q}_s$	Solid phase conductive heat flux [W]
Re	Reynolds number [$-$]
s_i	Specific entropy at the inlet [J/kgK]
s_o	Specific entropy at the outlet [J/kgK]
T	Temperature [K]
T_g	Gas temperature [K]
T_0	Temperature of the reference state [K]
$T_{CO_2,i}$	CO_2 inlet temperature [K]
$T_{CO_2,o}$	CO_2 outlet temperature [K]
T_{CO_2}	CO_2 temperature [K]
T_c	Temperature of the cold reservoir [K]
T_i	Temperature at the inlet [K]
T_o	Temperature at the outlet [K]
$T_{s,i}$	Initial solid phase temperature [K]
T_s	Solid phase temperature [K]
T_w	Wall temperature [K]
$\overline{T_s}$	Averaged solid phase temperature [K]
t	Time [s]
t_{fin}	Final time of the recovery [s]
t_{ini}	Initial time of the recovery [s]
t_r	Recovery time [s]

U_0/U_{mf}	Dimensionless gas superficial velocity [$-$]	
U_0	Superficial gas velocity [cm/s]	
U_{mf}	Minimum fluidization velocity [cm/s]	
V	Volume [m^3]	
$\vec{v}_g$	Gas velocity [m/s]	
$\vec{v}_s$	Solids velocity [m/s]	
W	Bed width [m]	
x	Horizontal coordinate [m]	
y	Vertical coordinate [m]	
$z_i g$	Specific potential energy at the inlet [J/kg]	
$z_o g$	Specific potential energy at the outlet [J/kg]	

Greek letters

α_g	Gas volume fraction [$-$]
α_s	Solids volume fraction [$-$]
$\Delta\dot{A}$	Increase of availability in the CO_2 [W]
Δs	Grid size in the computational domain [mm]
Δt_{rec}	Recovery time interval [s]
δ_b	Bubble fraction in the bed [$-$]
η_{Carnot}	Carnot efficiency [%]
η_{Ex}	Fractional exergetic efficiency [$-$]
γ_Θ	Collisional dissipation of Θ [m^2/s^2]
γ	Specific heats ratio [$-$]
μ_g	Gas viscosity [Pa s]
μ_s	Solids viscosity [Pa s]

$\overline{\overline{\tau}}_g$	Gas stress tensor [Pa]
$\overline{\overline{\tau}}_s$	Solids stress tensor [Pa]
Φ	Angle of internal friction [deg]
ρ_g	Gas density [kg/m^3]
ρ_s	Dense phase particle density [kg/m^3]
τ	Characteristic thermal time [s]
Θ	Granular temperature [m^2/s^2]

Acknowledgments

References

[1] M. Rodriguez-Sanchez, A. Sanchez-Gonzalez, D. Santana, Revised receiver efficiency of molten-salt power towers, Renewable and Sustainable Energy Reviews 52 (2015) 1331 – 1339.

[2] C. K. Ho, A review of high-temperature particle receivers for concentrating solar power, Applied Thermal Engineering 109, Part B (2016) 958 – 969. Special Issue: Solar Energy Research Institute for India and the United States (SERIIUS) – Concentrated Solar Power.

[3] C. K. Ho, B. D. Iverson, Review of high-temperature central receiver designs for concentrating solar power, Renewable and Sustainable Energy Reviews 29 (2014) 835 – 846.

[4] S. Besarati, D. Goswami, 8 - supercritical CO_2 and other advanced power cycles for concentrating solar thermal (CST) systems, in: M. J. Blanco, L. R. Santigosa (Eds.), Advances in Concentrating Solar Thermal Research and Technology, Woodhead Publishing Series in Energy, Woodhead Publishing, 2017, pp. 157 – 178. doi:https://doi.org/10.1016/B978-0-08-100516-3.00008-3.

[5] F. Crespi, G. Gavagnin, D. Sánchez, G. S. Martínez, Supercritical carbon dioxide cycles for power generation: A review, Applied Energy 195 (2017) 152 – 183.

[6] R. Singh, S. A. Miller, A. S. Rowlands, P. A. Jacobs, Dynamic characteristics of a direct-heated supercritical carbon-dioxide brayton cycle in a solar thermal power plant, Energy 50 (2013) 194 – 204.

[7] Y. Ahn, S. J. Bae, M. Kim, S. K. Cho, S. Baik, J. I. Lee, J. E. Cha, Review of supercritical CO_2 power cycle technology and current status of research and development, Nuclear Engineering and Technology 47 (2015) 647 – 661.

[8] F. Crespi, D. Sánchez, J. M. Rodríguez, G. Gavagnin, Fundamental thermo-economic approach to selecting sCO$_2$ power cycles for CSP applications, Energy Procedia 129 (2017) 963 – 970.

[9] J. Ortega, S. Khivsara, J. Christian, C. Ho, P. Dutta, Coupled modeling of a directly heated tubular solar receiver for supercritical carbon dioxide brayton cycle: Structural and creep-fatigue evaluation, Applied Thermal Engineering 109 (2016) 979 – 987. Special Issue: Solar Energy Research Institute for India and the United States (SERIIUS) – Concentrated Solar Power.

[10] T. Neises, C. Turchi, A comparison of supercritical carbon dioxide power cycle configurations with an emphasis on CSP applications, Energy Procedia 49 (2014) 1187 – 1196.

[11] R. Chacartegui, J. M. de Escalona, D. Sánchez, B. Monje, T. Sánchez, Alternative cycles based on carbon dioxide for central receiver solar power plants, Applied Thermal Engineering 31 (2011) 872 – 879. MNF 2009 Special Issue.

[12] K. Wang, M.-J. Li, J.-Q. Guo, P. Li, Z.-B. Liu, A systematic comparison of different s-CO$_2$ brayton cycle layouts based on multi-objective optimization for applications in solar power tower plants, Applied Energy 212 (2018) 109 – 121.

[13] J. D. Osorio, R. Hovsapian, J. C. Ordonez, Dynamic analysis of concentrated solar supercritical CO$_2$-based power generation closed-loop cycle, Applied Thermal Engineering 93 (2016) 920 – 934.

[14] J. Liu, H. Chen, Y. Xu, L. Wang, C. Tan, A solar energy storage and power generation system based on supercritical carbon dioxide, Renewable Energy 64 (2014) 43 – 51.

[15] Y. Zhang, K. Yang, H. Hong, X. Zhong, J. Xu, Thermodynamic analysis of a novel energy storage system with carbon dioxide as working fluid, Renewable Energy 99 (2016) 682 – 697.

[16] E. Johnson, L. Bates, A. Dower, P. C. Bueno, R. Anderson, Thermal energy storage with supercritical carbon dioxide in a packed bed: Modeling charge-discharge cycles, The Journal of Supercritical Fluids 137 (2018) 57 – 65.

[17] U. Pelay, L. Luo, Y. Fan, D. Stitou, M. Rood, Thermal energy storage systems for concentrated solar power plants, Renewable and Sustainable Energy Reviews 79 (2017) 82 – 100.

[18] M. Hänchen, S. Brückner, A. Steinfeld, High-temperature thermal storage using a packed bed of rocks – heat transfer analysis and experimental validation, Applied Thermal Engineering 31 (2011) 1798 – 1806.

[19] G. Zanganeh, A. Pedretti, A. Haselbacher, A. Steinfeld, Design of packed bed thermal energy storage systems for high-temperature industrial process heat, Applied Energy 137 (2015) 812 – 822.

[20] R. Anderson, L. Bates, E. Johnson, J. F. Morris, Packed bed thermal energy storage: A simplified experimentally validated model, Journal of Energy Storage 4 (2015) 14 – 23.

[21] F. Opitz, P. Treffinger, Packed bed thermal energy storage model – generalized approach and experimental validation, Applied Thermal Engineering 73 (2014) 245 – 252.

[22] M. Cascetta, G. Cau, P. Puddu, F. Serra, A comparison between CFD simulation and experimental investigation of a packed-bed thermal energy storage system, Applied Thermal Engineering 98 (2016) 1263 – 1272.

[23] Z. Ma, G. Glatzmaier, M. Mehos, Fluidized bed technology for concentrating solar power with thermal energy storage, Journal of Solar Energy Engineering, Transactions of the ASME 136 (2014).

[24] E. Alonso, M. Romero, Review of experimental investigation on directly irradiated particles solar reactors, Renewable and Sustainable Energy Reviews 41 (2015) 53 – 67.

[25] G. Flamant, D. Gauthier, H. Benoit, J.-L. Sans, R. Garcia, B. Boissière, R. Ansart, M. Hemati, Dense suspension of solid particles as a new heat transfer fluid for concentrated solar thermal plants: On-sun proof of concept, Chemical Engineering Science 102 (2013) 567 – 576.

[26] H. Benoit, I. P. López, D. Gauthier, J.-L. Sans, G. Flamant, On-sun demonstration of a 750˚C heat transfer fluid for concentrating solar systems: Dense particle suspension in tube, Solar Energy 118 (2015) 622 – 633.

[27] P. García-Triñanes, J. Seville, B. Boissière, R. Ansart, T. Leadbeater, D. Parker, Hydrodynamics and particle motion in upward flowing dense particle suspensions: Application in solar receivers, Chemical Engineering Science 146 (2016) 346 – 356.

[28] R. Ansart, P. García-Triñanes, B. Boissière, H. Benoit, J. P. Seville, O. Simonin, Dense gas-particle suspension upward flow used as heat transfer fluid in solar receiver: PEPT experiments and 3D numerical simulations, Powder Technology 307 (2017) 25 – 36.

[29] M. A. Reyes-Belmonte, F. Gómez-García, J. González-Aguilar, M. Romero, H. Benoit, G. Flamant, Heat exchanger modelling in central receiver solar power plant using dense particle suspension, AIP Conference Proceedings 1850 (2017)

030042.

[30] H. Zhang, H. Benoit, I. Perez-Lopèz, G. Flamant, T. Tan, J. Baeyens, High-efficiency solar power towers using particle suspensions as heat carrier in the receiver and in the thermal energy storage, Renewable Energy 111 (2017) 438 − 446.

[31] M. Poletto, P. Salatino, L. Massimilla, Fluidization of solids with CO_2 at pressures and temperatures ranging from ambient to nearly critical conditions, Chemical Engineering Science 48 (1993) 617 − 621.

[32] A. Marzocchella, P. Salatino, Fluidization of solids with CO_2 at pressures from ambient to supercritical, AIChE Journal 46 (2000) 901–910.

[33] C. Vogt, R. Schreiber, G. Brunner, J. Werther, Fluid dynamics of the supercritical fluidized bed, Powder Technology 158 (2005) 102 − 114. Prof. Dr.-Ing. Otto Molerus 70th birthday.

[34] L. Wei, Y. Lu, Fluidization of solids with water in supercritical conditions − characteristics of pressure fluctuations, Chemical Engineering Research and Design 109 (2016) 657 − 666.

[35] Y. Lu, T. Zhang, X. Dong, Bed to wall heat transfer in supercritical water fluidized bed: Comparison with the gas–solid fluidized bed, Applied Thermal Engineering 88 (2015) 297 − 305. Special Issue for International Heat Transfer Symposium 2014.

[36] S. Rodríguez-Rojo, M. Cocero, Supercritical fluidized bed modeling, The Journal of Supercritical Fluids 50 (2009) 54 − 60.

[37] W. Yang, Handbook of Fluidization and Fluid-Particle Systems, Chemical Industries, Taylor & Francis, 2003.

[38] S. Oka, Fluidized Bed Combustion, Mechanical Engineering, CRC Press, 2003.

[39] O. Levenspiel, Design of long heat regenerators by use of the dispersion model, Chemical Engineering Science 38 (1983) 2035 − 2045.

[40] A. M. El-Halwagi, M. A. El-Rifal, M. M. El-Halwagi, Mathematical modeling of fluidized bed heat regenerators, Chemical Engineering Communications 72 (1988) 121–139.

[41] M. Haid, H. Martin, H. Müller-Steinhagen, Heat transfer to liquid—solid fluidized beds, Chemical Engineering and Processing: Process Intensification 33 (1994) 211 − 225.

[42] S. Shahhosseini, S. S. Khademi, M. A. Sobati, A novel PFBHE (periodic fluidized bed heat exchanger): Introduction and preliminary performance evaluation, Energy 107 (2016) 443 − 452.

[43] M. Ehsani, S. Movahedirad, S. Shahhosseini, The effect of particle properties on the heat transfer characteristics of a liquid–solid fluidized bed heat exchanger, International Journal of Thermal Sciences 102 (2016) 111 − 121.

[44] M. Tan, R. Karabacak, M. Acar, Experimental assessment the liquid/solid fluidized bed heat exchanger of thermal performance: An application, Geothermics 62 (2016) 70 − 78.

[45] Z. Y. Zhou, A. B. Yu, P. Zulli, Particle scale study of heat transfer in packed and bubbling fluidized beds, AIChE Journal 55 (2009) 868–884.

[46] S. Al-Arkawazi, Modeling the heat transfer between fluid-granular medium, Applied Thermal Engineering 128 (2018) 696 − 705.

[47] J. Chao, J. Lu, H. Yang, M. Zhang, Q. Liu, Experimental study on the heat transfer coefficient between a freely moving sphere and a fluidized bed of small particles, International Journal of Heat and Mass Transfer 80 (2015) 115 − 125.

[48] A. V. Patil, E. Peters, V. S. Sutkar, N. Deen, J. Kuipers, A study of heat transfer in fluidized beds using an integrated dia/piv/ir technique, Chemical Engineering Journal 259 (2015) 90 − 106.

[49] T. Lichtenegger, E. Peters, J. Kuipers, S. Pirker, A recurrence CFD study of heat transfer in a fluidized bed, Chemical Engineering Science 172 (2017) 310 − 322.

[50] L. Lu, A. Morris, T. Li, S. Benyahia, Extension of a coarse grained particle method to simulate heat transfer in fluidized beds, International Journal of Heat and Mass Transfer 111 (2017) 723 − 735.

[51] J. A. M. Kuipers, K. J. Van Duin, F. P. H. Van Beckum, W. P. M. Van Swaaij, A numerical model of gas-fluidized beds,

Chemical Engineering Science 47 (1992) 1913 – 1924.

[52] D. Gidaspow, Multiphase flow and Fluidization: Continuum and kinetic theory descriptions, Academic Press, San Diego, CA, 1994.

[53] B. G. M. van Wachem, A. E. Almstedt, Methods for multiphase computational fluid dynamics, Chemical Engineering Journal 96 (2003) 81 – 98.

[54] N. G. Deen, M. Van Sint Annaland, M. A. Van der Hoef, J. A. M. Kuipers, Review of discrete particle modeling of fluidized beds, Chemical Engineering Science 62 (2007) 28 – 44.

[55] C. R. Müller, D. J. Holland, A. J. Sederman, S. A. Scott, J. S. Dennis, L. F. Gladden, Granular temperature: Comparison of magnetic resonance measurements with discrete element model simulations, Powder Technology 184 (2008) 241 – 253.

[56] F. Hernández-Jiménez, L. M. Garcia-Gutierrez, A. Soria-Verdugo, A. Acosta-Iborra, Fully coupled TFM-DEM simulations to study the motion of fuel particles in a fluidized bed, Chemical Engineering Science 134 (2015) 57 – 66.

[57] L. Garcia-Gutierrez, F. Hernández-Jiménez, E. Cano-Pleite, A. Soria-Verdugo, Improvement of the simulation of fuel particles motion in a fluidized bed by considering wall friction, Chemical Engineering Journal 321 (2017) 175 – 183.

[58] J. R. Grace, F. Taghipour, Verification and validation of CFD models and dynamic similarity for fluidized beds, Powder Technology 139 (2004) 99 – 110.

[59] J. R. Grace, T. Li, Complementarity of CFD, experimentation and reactor models for solving challenging fluidization problems, Particuology 8 (2010) 498 – 500.

[60] M. Syamlal, W. Rogers, T. J. O'Brien, MFIX Documentation: Theory Guide, U.S. Department of Energy (DOE), Morgantown Energy Technology Center, Morgantown, West Virginia, 1993.

[61] S. Benyahia, M. Syamlal, T. J. O'Brien, Summary of MFIX equations 2005-4, 2007.

[62] R. Beetstra, M. van der Hoef, J. Kuipers, Numerical study of segregation using a new drag force correlation for polydisperse systems derived from lattice-boltzmann simulations, Chemical Engineering Science 62 (2007) 246 – 255. Fluidized Bed Applications.

[63] D. Gunn, Transfer of heat or mass to particles in fixed and fluidised beds, International Journal of Heat and Mass Transfer 21 (1978) 467 – 476.

[64] K. Buist, B. Backx, N. Deen, J. Kuipers, A combined experimental and simulation study of fluid-particle heat transfer in dense arrays of stationary particles, Chemical Engineering Science 169 (2017) 310 – 320.

[65] J. Kuipers, W. Prins, W. van Swaaij, Numerical calculation of wall-to-bed heat transfer coefficients in gas-fluidized beds, AIChE journal 38 (1992) 1079–1091.

[66] A. Burcat, B. Ruscic, Third Millenium Ideal Gas and Condensed Phase Thermochemical Database for Combustion with Updates from Active Thermochemical Tables, Anl [series], Argonne National Laboratory, 2005.

[67] N. P. Siegel, M. D. Gross, R. Coury, The development of direct absorption and storage media for falling particle solar central receivers, Journal of Solar Energy Engineering 137 (2015) 041003 – 041003–7.

[68] T. Li, J. R. Grace, X. Bi, Study of wall boundary condition in numerical simulations of bubbling fluidized beds, Powder Technology 203 (2010) 447 – 457.

[69] F. Hernández-Jiménez, J. Third, A. Acosta-Iborra, C. Müller, Comparison of bubble eruption models with two-fluid simulations in a 2D gas-fluidized bed, Chemical Engineering Journal 171 (2011) 328 – 339.

[70] S. Ergun, Fluid flow through packed columns, Fluid Flow Through Packed Columns (1952) 89–94.

[71] C. Y. Wen, Y. H. Yu, A generalized method for predicting the minimum fluidization velocity, AIChE Journal 12 (1966) 610–612.

[72] P. Carman, Trans. insin. chem. engrs, J. Soc. Chem. Industr 15 (1937) 150.

[73] J. Grace, G. Hetsroni, Handbook of multiphase systems, Hetsroni MG Edition, Hemisphere, New York (1982).

[74] T. Li, Validation of a 2.5D CFD model for cylindrical gas–solids fluidized beds, Powder Technology 286 (2015) 817 – 827.

[75] S. Besarati, D. Goswami, 8 - supercritical CO_2 and other advanced power cycles for concentrating solar thermal (CST) systems, in: M. J. Blanco, L. R. Santigosa (Eds.), Advances in Concentrating Solar Thermal Research and Technology, Woodhead Publishing Series in Energy, Woodhead Publishing, 2017, pp. 157 – 178. doi:`https://doi.org/10.1016/B978-0-08-100516-3.00008-3`.

[76] P. Garg, P. Kumar, K. Srinivasan, Supercritical carbon dioxide brayton cycle for concentrated solar power, The Journal of Supercritical Fluids 76 (2013) 54 – 60.

[77] P. Kumar, K. Srinivasan, Carbon dioxide based power generation in renewable energy systems, Applied Thermal Engineering 109, Part B (2016) 831 – 840. Special Issue: Solar Energy Research Institute for India and the United States (SERIIUS) – Concentrated Solar Power.

[78] M. J. Moran, H. N. Shapiro, Fundamentals of engineering thermodynamics, 6 ed., John Wiley and Sons Inc., New York, NY, 2009.

[79] D. Kunii, O. Levenspiel, Fluidization Engineering, 2nd ed., Butterworth-Heinemann, Boston, 1991.

[80] J. Sánchez-Prieto, A. Soria-Verdugo, J. Briongos, D. Santana, The effect of temperature on the distributor design in bubbling fluidized beds, Powder Technology 261 (2014) 176 – 184.